

Chapter 2

Particle Dispersion and Mass Transfer in Turbulent Shear Flows

Abstract DNS of condensation mass transfer in particle-laden incompressible turbulent mixing layers are performed. The flows are comprised of a particle-free condensable vapor mixing with micron-size porous particles. Simulations are performed at a single Reynolds number while varying the particle Stokes number, the mass transfer and convective time scales, and the vapor concentration at the particle surface. Convection-enhanced mass transfer and the surface concentration at the gas/particle interface are of great importance in accurately predicting gas–particle mass transfer rates. Particle slip velocities are varied by considering different particle Stokes numbers. Simulations utilizing the “perfect sink” assumption are compared with simulations in which the non-zero, steady-state surface concentration is calculated taking into account the sorption properties of porous particles. Results indicate that particle dispersion is greater at lower particle Stokes numbers. However the increased particle slip velocity in the higher particle Stokes number flows result in increased condensation. Furthermore, results show that the perfect sink assumption leads to an overprediction in the condensation mass transfer rate.

2.1 Strategies for Sorption Modeling in Turbulent Flows

Gas-to-particle mass transfer in turbulent flows is not very well understood. Little physical data is available from full-scale tests. Numerical simulation of condensation mass transfer in turbulent particle-laden flows can improve our understanding of the underlying dynamics and transport processes as well as provide useful knowledge and guidance in the design and performance of the so-called virtual sorbent beds.

A large number of computational studies of condensation mass transfer rely on assumptions which are rather restrictive, or questionable, when made, or applied, in the context of turbulent flows. One such assumption concerns the vapor/gas concentration at the particle surface. The perfect sink assumption, for instance, implies that the concentration of condensable vapor at the particle surface is identically zero [16–18]. Consequently, mass transfer resistances associated with intra-particle diffusion and sorption kinetics are neglected. For that matter, the

vapor concentration at the fluid–particle interface is of critical importance. An analytical expression for the concentration may be obtained under the assumption of steady-state pore diffusion [5, 43, 88, 118]. These expressions are valid over a wide time range and remove the need to solve the species transport equation within the particles. Of great concern is the physics/dynamics at the fluid–particle interface. From a flow physics perspective, the mass transfer depends on the fluid velocity at the particle surface. Research has shown that the gas–particle slip velocity grows linearly with the particle Stokes number [95]. More specifically, researchers have identified regions of positive and negative slip velocities related to accelerating and decelerating fluid regions, respectively [49, 73]. Although the presence of the particle slip velocity enhances mass transfer rates [32, 39, 81, 82, 120], it has been neglected in several studies [29, 72, 97–99]. The presence of fluctuating scalar/chemical and particle fields in turbulent flows, and the resultant variation in residence times, suggests that modeling of the temporally and spatially varying fluid–particle dynamics would improve our predictive ability [13, 18, 24, 99, 116].

Particle dispersion in turbulent flows has been studied extensively in the past several decades [3, 10, 11, 52, 55, 61, 68, 74, 76, 77, 107, 111, 115]. DNS was used to investigate the effect of isotropic turbulence on the particle concentration and identify flow regions that significantly influence particle transport and mixing [107]. The computational expense of DNS renders it prohibitive for simulation of practical flows. Methods such as LES and RANS are commonly used to model fluid flow in more complex geometries [3, 52, 68, 89, 111]. In performing LES or RANS, only the large-scale or mean fluid motion is resolved, and the effects of the small-scale fluctuations on particle dispersion and condensation are largely unknown [38, 80]. Good agreement was found between experiments and DNS of inertial particle clustering in a three-dimensional, isotropic turbulence field, suggesting that three-dimensional simulations are needed to accurately describe particle motion in turbulent flows [92]. It has been reported that the use of LES may result in significant errors in predicting particle motion for Stokes numbers around unity [74]. Additionally, modeling efforts of particle-laden flows with condensation have thus far neglected the effects of turbulence on condensation or have been otherwise un-validated [68].

We consider the condensation of vapor onto micron-size particles in turbulent mixing layers. The motivation is twofold: to elucidate the effects of different flow/particle parameters on condensation mass transfer in turbulent flows and to establish datasets that may be used in evaluating the performance of turbulence models (in the contexts of LES and RANS). Several nondimensional parameters are varied to consider the effects of (1) the “driving” force or concentration difference between the particle, and the fluid is varied, (2) mass transfer across the particle, and (3) particle dispersion on condensation mass transfer.

2.2 Formulation

2.2.1 Fluid Field

The flows under consideration are described by the incompressible Navier–Stokes equations. The primary transport variables are the fluid velocity, u_i , and the fluid pressure, p . These variables are governed by the conservation of mass and momentum equations

$$\frac{\partial u_j}{\partial x_j} = 0, \quad (2.1)$$

$$\frac{\partial u_i}{\partial t} + \frac{\partial u_i u_j}{\partial x_j} = -\frac{\partial p}{\partial x_i} + \frac{1}{Re_L} \frac{\partial^2 u_i}{\partial x_j \partial x_j}, \quad (2.2)$$

where Re_L is the Reynolds number. The transport of a condensable vapor is given by

$$\frac{\partial Y_i}{\partial t} + \frac{\partial u_j Y_i}{\partial x_j} = \frac{1}{Re_L Sc} \frac{\partial^2 Y_i}{\partial x_j \partial x_j}, \quad (2.3)$$

where Y_i is the mass fraction of species i and Sc is the Schmidt number.

2.2.2 Particle Field

The equations describing the particle trajectories are

$$\frac{dx_{i,p}}{dt} = u_{i,p}, \quad \frac{du_{i,p}}{dt} = \frac{f_p}{St_k} (u_i - u_{i,p}) \quad (2.4)$$

where $x_{i,p}$ is the particle location, $u_{i,p}$ is the particle velocity in the x_i direction, f_p is the drag correction factor,

$$St_k = \frac{d_p^2 \rho_p}{18 \mu} \times \frac{U_o}{L}, \quad (2.5)$$

is the particle Stokes number, d_p is the particle diameter, ρ_p is the particle bulk density, μ is the dynamic fluid viscosity, L is the reference length, and U_o is the reference velocity [3, 30, 61, 76, 78]. The drag correction factor, f_p , accounts for increased drag in the outer Stokesian region due to vortex shedding in the wake of the particle and is given by

$$f_p = 1 + 0.15 Re_p^{0.687}, \quad (2.6)$$

where $Re_p = |\Delta u_i|Re_{po}$ is the particle Reynolds number and $Re_{po} = d_p U_o / \nu$, where ν is the kinematic viscosity [41]. The ratio St_k/f_p is also referred to as a nondimensional particle relaxation time, describing the ability of a particle to adjust to the surrounding fluid [3]. Buoyancy forces, added mass effects, and Basset forces are neglected, as well as pressure gradients and shear forces across the length of the particles [55]. The particle volume fraction and mass loadings are assumed to be sufficiently low to neglect particle–particle interactions; the dynamics of the flow are not modified by the presence of particles [76, 77]. All particles are assumed rigid spheres, the diameter of which is much larger than the gas mean free path.

2.2.3 Gas-to-Particle Mass Transfer

The condensable vapor is transferred from the fluid to the particle surface by convection and diffusion. The particle mass growth rate is equal to the mass flow rate toward a single particle and is given by

$$\frac{dm_p}{dt} = A \frac{Sh}{2} Y(1 - c_s), \quad (2.7)$$

where m_p is the particle mass (nondimensionalized by the mass of vapor initially contained in volume L^3), Sh is the Sherwood number, c_s is the vapor concentration at the particle surface, and the parameter A is given by $A = (k_{mo} d_p^2 \pi) / (U_o L^2)$, in which k_{mo} is the external mass transfer coefficient in a quiescent fluid. The parameter A represents the ratio of diffusive mass transfer to the particle surface and advective mass transfer in the bulk flow. It is the product of a dimensionless velocity, k_{mo}/U_o , and a dimensionless area, $d_p^2 \pi / L^2$, and can be written in terms of nondimensional groups as $A = (2\pi Re_{po}) / (Sc Re_L^2)$. For $A \ll 1$ advection is the dominant mode of mass transfer in the particle-laden flow. The Sherwood number is the ratio of the mass transfer rate at the fluid–particle interface to the diffusive mass transfer rate in the fluid and accounts for the increased mass transfer due to convective effects at the particle surface. The augmentation in mass transfer is due to the presence of a particle slip velocity. We adopt a semiempirical correlation for Sh , first proposed by Frössling [32], who showed analytically that the Sherwood number is proportional to $Re_p^{1/2} Sc^{1/3}$:

$$Sh = 2 + 0.552 Re_p^{1/2} Sc^{1/3}, \quad (2.8)$$

The expression was developed using experimental data for evaporating drops and was later used in the context of gas–particle mass transfer [17, 18, 29, 68]. If the particle is treated as a perfect sink, the surface concentration vanishes (that is, $c_s = 0$). Conversely, if the vapor concentration at the particle surface is equal to

the vapor concentration in the surrounding fluid, c_s is equal to unity, and there is no mass transfer. For the case where neither assumption is valid, the concentration at the surface is given by

$$c_s = \frac{Bi_m}{Bi_m + \Phi / \tanh \Phi - 1}, \quad \Phi = \sqrt{\frac{q_{\max}(1 - \epsilon_p)k_1(d_p/2)^2}{\mathcal{D}_{\text{eff}}}}, \quad (2.9)$$

where Φ is the Thiele number, $Bi_m = Bi_{mo}Sh/2$ is the Biot number for mass transfer, $Bi_{mo} = (k_{mo}d_p/2)/\mathcal{D}_{\text{eff}}$ is the reference mass Biot number, and \mathcal{D}_{eff} is the effective pore diffusivity [5, 43, 72, 83, 97, 110, 118]. The mass Biot number is the ratio of the mass transfer rate at the fluid–particle interface to the diffusive mass transfer rate inside the macropores. For spherical particles, the external mass transfer coefficient in a stagnant fluid is given by $k_{mo} = \mathcal{D}/(d_p/2)$, where \mathcal{D} is the molecular diffusivity of the condensable vapor. The Thiele number is the ratio of the adsorption rate at the pore walls to the diffusive mass transfer rate inside the macropores [22, 54, 110]. In the context of the Langmuir theory—used to describe the adsorption of vapor molecules from the macropores to the solid structure of the particle—the Thiele number is parameterized by the maximum concentration in the solid, q_{\max} ; the particle porosity, ϵ_p (defined as the total pore volume divided by the particle volume); and the adsorption rate coefficient, k_1 . For $\Phi \gg 1$ the adsorption rate is much larger than the diffusion rate, and a vapor molecule is likely to be absorbed before it can diffuse far into the macroporous structure of the particle. It is assumed that the adsorbed phase concentration in the solid is much smaller than the maximum uptake capacity and that the macropore concentration reaches a quasi-steady state instantly [43, 118]. All particles are assumed to be homogeneous macroporous structures with a finite uptake capacity [87].

2.3 Particle Injection Through a Round Nozzle

During ACI, PAC flows into the highly turbulent flue gas where it adsorbs gas-phase mercury. We simulate the flow of microscale particles through a round nozzle in an isothermal ($T = 300$ K) flow. The Reynolds number is $Re_D = 3000$; the computational domain is $12D \times 8D \times 8D$ in the x , y , and z directions and is covered by a grid comprised of $1024 \times 640 \times 640$ points. The resolution is clustered in the neighborhood of the shear layers to ensure grid-independent results.

2.3.1 Particle Dispersion

The fluid–particle field downstream of a nozzle [used for ACI] is shown in Fig. 2.1. The image shows an instantaneous view of $d_p = 0.1 \mu\text{m}$, $d_p = 1 \mu\text{m}$, and $d_p = 10 \mu\text{m}$ particles and near vortices downstream of the nozzle. The vortices form as the

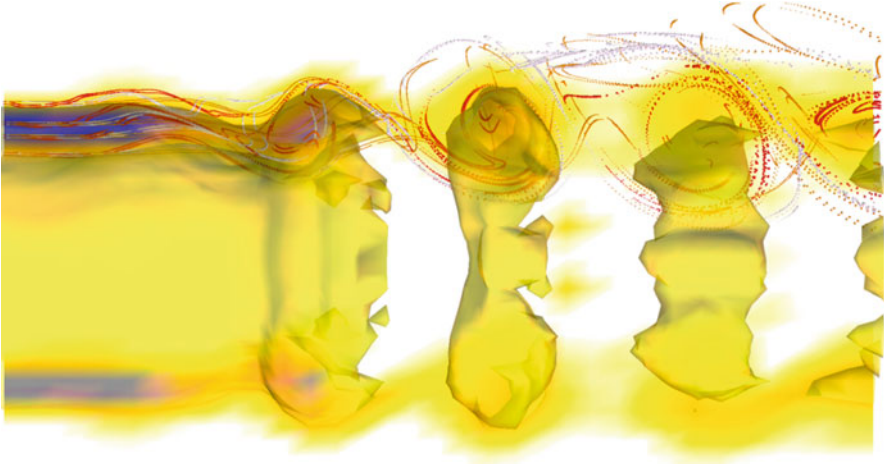


Fig. 2.1 Instantaneous micro-particle streak lines in the neighborhood of vortex rings

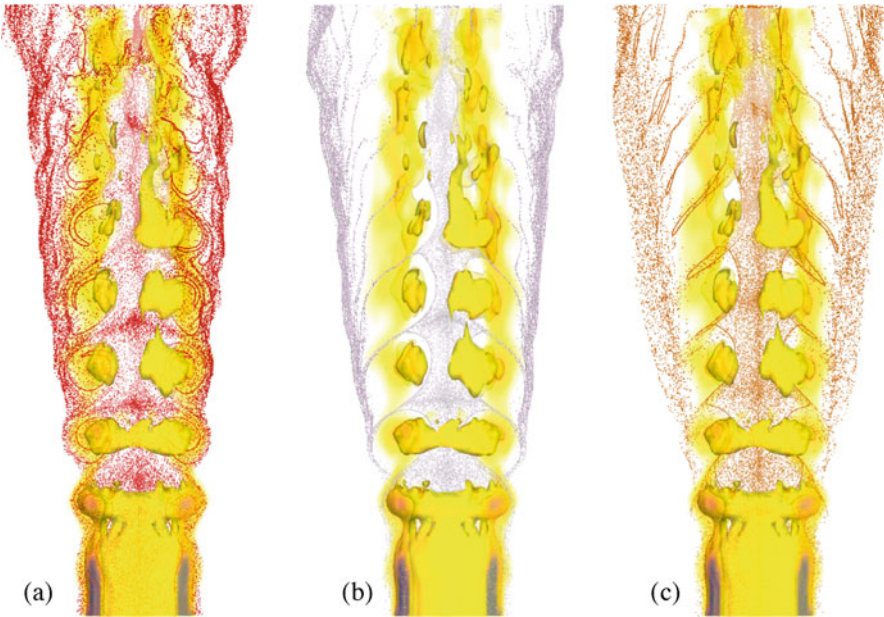


Fig. 2.2 Instantaneous snapshot of particle locations: (a) $0.1 \mu\text{m}$; (b) $1 \mu\text{m}$, and (c) $10 \mu\text{m}$

jet transitions from a laminar flow to a turbulent one. The particle traces indicate that the particles have different trajectories. This is more clearly observed in Fig. 2.2. For clarity, and the purposes of illustration, roughly 10,000 particles are shown in each image. As the flow travels downstream, the jet entrains the background fluid, and

the particles are dispersed. (In the case of ACI, the background fluid would be flue gas containing mercury vapor.) Figure 2.2a shows that the $d_p = 0.1 \mu\text{m}$ particles are fairly well dispersed across the jet, with particles present near the centerline, in the eddies, and at the jet periphery. However the image reveals that particles are accumulating at the outer part of the flow, indicating that a large number of the smaller $0.1 \mu\text{m}$ particles have crossed into the slower-moving background flue gas. These particles are relatively inertialess and follow the fluid. Figure 2.2b shows a similar distribution pattern for the $1 \mu\text{m}$ particles. There are particles located in the core of the jet, and there is accumulation at the periphery. However the vortex cores are virtually devoid of the $1 \mu\text{m}$ particles, the vortices that transported all particles in their vicinity into the slower-moving background fluid. A snapshot of the largest $10 \mu\text{m}$ diameter particles shown in Fig. 2.2c reveals that fewer particles have made it into the background fluid. While most particles are found along the jet centerline, some are in the process of being “flung” across the vortex cores. Turbulent mixing, including large-scale mixing via eddies, can greatly increase the residence or contact time between the particles and the background condensable vapor and thus adsorption.

2.3.2 Particle Reynolds Number

The particle velocities and trajectories are a function of the drag, the Stokes number, and the slip velocity. While the Stokes number is fixed, the drag correction factor is a function of the particle Reynolds number, $Re_p = |u_i - u_{i,p}|Re_{po}$. Similarly, the mass transfer rate is given by the Sherwood number and is a function of the particle Reynolds number. Histograms of the particle Reynolds number for the 0.1 , 1 , and $10 \mu\text{m}$ diameter particles are shown in Fig. 2.3a. The figure shows a unimodal distribution of particle Reynolds numbers for the $0.1 \mu\text{m}$ diameter particles, with

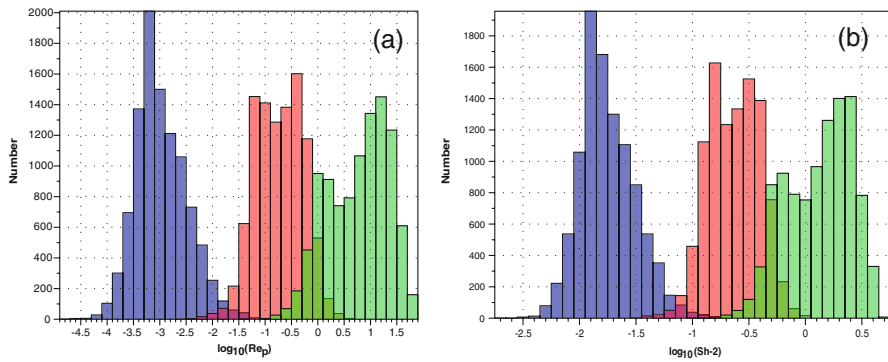


Fig. 2.3 Instantaneous distributions of (a) particle Reynolds number, Re_p , and (b) Sherwood number, Sh , with a function of particle diameter ($0.1 \mu\text{m}$ particles in blue, $1 \mu\text{m}$ particles in red, and $10 \mu\text{m}$ particles in green)

mean values around $Re_p = 0.001$. There are three readily observed trends. First, as the particle size increases, the distribution of Re_p values moves to the right. The mean particle Reynolds number for the $1\text{ }\mu\text{m}$ and $10\text{ }\mu\text{m}$ diameter particles is roughly $Re_p = 0.25$ and $Re_p = 5$, respectively. These increasing values show that as the particles get larger, more mercury vapor is adsorbed onto their surface. The second trend is that as the particles get larger, the distribution moves from a unimodal (for the $0.1\text{ }\mu\text{m}$ particles) to bimodal ($10\text{ }\mu\text{m}$ particles). (The $1\text{ }\mu\text{m}$ particles show a more broad unimodal distribution.) A small tail develops as the distribution moves to the right—roughly at $Re_p = 1$ for the $10\text{ }\mu\text{m}$ particles. This value is much lower than the peak value and suggests that these particles are moving more slowly relative to the fluid. That is, they have overcome their initial inertia and moving “with” the fluid, compared to the particles with larger particle Reynolds numbers. The third trend observed is that most particles experience lower particle Reynolds numbers. These trends are also observed in the Sherwood number. As Sh shifts farther right, the count decreases. This reveals that fewer particles experience the high gas-to-particle mass transfer conditions.

Obtaining a more quantitative view of the mass transfer dynamics is difficult because of the compute time. The particle residence time in the computational domain is on tens of milliseconds. As a result, the time that the particles and background gas is relatively low. Each computation of the jet flow required roughly 2×10^5 CPU-hours.

2.4 Multiphase Mixing Layer Transport

Simulations of temporal mixing layers are performed to obtain a more detailed view of the fluid–particle mixing. The configuration is such that the upper half of the mixing layer contains mercury vapor, while the lower half contains the microscale particles. As the flow develops, the two streams come into contact, and condensation occurs. A reference frame is attached to the fluid and moves with the mean velocity, as shown in Fig. 2.4. In doing so, the simulation is transformed from a spatially developing one to a temporally developing one. The flows under consideration are

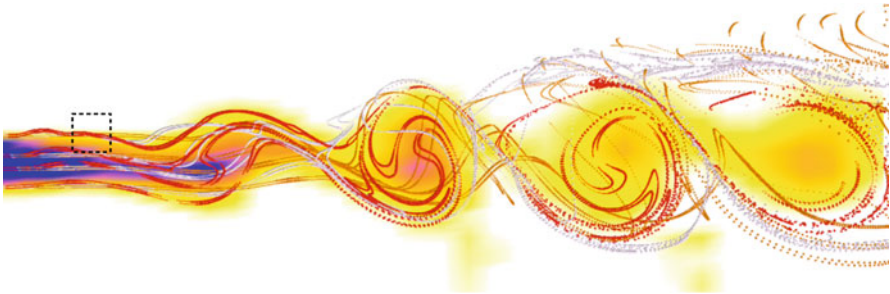
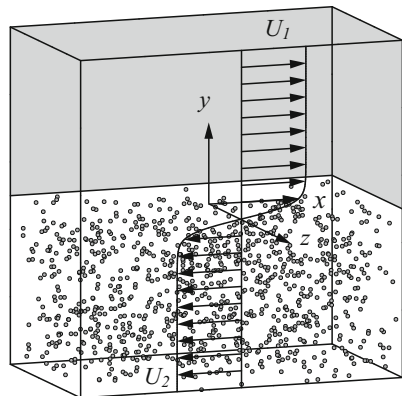


Fig. 2.4 Particle field close-up indicating area for temporal flow simulation

Fig. 2.5 Particle-laden temporal mixing layer flow configuration



three-dimensional incompressible mixing layers. A temporal mixing layer is formed when two parallel streams which travel in opposite direction meet [75, 96]. The streams mix and entrain fluid through large-scale coherent structures [9, 12, 85]). The spatial coordinates are $\mathbf{x} = (x, y, z)$ in streamwise, cross-stream, and spanwise directions, respectively, as shown in Fig. 2.5. The corresponding velocities are $\mathbf{u} = (u, v, w)$. Initially, the upper stream contains condensable vapor, and the lower stream contains uniformly distributed particles. As the flow evolves in time, vapor and particles are mixed, and mass is transferred from the gas phase to the particle phase through condensation.

2.4.1 Physical Parameters

The Reynolds number for all flows is $Re_L = 450$ and is based on the initial 99%-boundary layer thickness, $L = \delta$, and one half of the velocity difference across the two streams $U_o = 0.5 \times (U_1 - U_2)$. The Schmidt number for the condensable vapor is $Sc = 1.1$. To elucidate the effect of the governing parameters, six simulations are performed for different values of the reference particle Reynolds number, Re_{po} ; the parameter A ; the particle Stokes number, St_k ; the reference mass Biot number, Bi_{mo} ; and the Thiele number, Φ , as listed in Table 2.1. Case 1a is the base case, representing typical operating conditions of an ESP where carbon particles with diameter $d_p = 10 \mu\text{m}$ are used to remove mercury vapor from flue gas at atmospheric pressure and a temperature of $T = 500 \text{ K}$ [17, 18]. Activated carbon particles of type Darco® G60 are considered, which have a porosity of $\epsilon_p = 0.65$ and a bulk density of $\rho_p = 450 \text{ kg/m}^3$ [45, 46, 97–99]. Starting from case 1a, the governing parameters are changed separately. In case 2, the parameter A is set to $A = 10^{-3}$; the reference particle Reynolds number is $Re_{po} = 25.3$, since A and Re_{po} are not independent and the Reynolds and Schmidt number remain unchanged

Table 2.1 Simulation parameters for cases 1a–d, case 2, and case 3

Case	1a	1b	1c	1d	2	3
Particle Reynolds number, Re_{po}	1.32	1.32	1.32	1.32	25.3	1.32
Parameter A ($\times 10^5$)	5.2	5.2	5.2	5.2	100	5.2
Stokes number, St_k	0.17	0.17	0.17	0.17	0.17	10.0
Mass Biot number, Bi_{mo}	0	10	181	181	0	0
Thiele number, Φ	∞	10	10	0.2	∞	∞

in all simulations. Case 3 differs from case 1a in that the particle Stokes number is increased from $St_k = 0.17$ to $St_k = 10$. Mass transfer resistances associated with intra-particle diffusion and sorption kinetics are neglected altogether in cases 1a, 2, and 3. That is, particles are assumed to be perfect sinks, which mathematically corresponds to $Bi_{mo} \rightarrow 0$ and/or $\Phi \rightarrow \infty$. Cases 1b, 1c, and 1d are derived from case 1a. The perfect sink assumption, however, is dropped and (2.9) is used to compute the non-zero surface concentration. In case 1b, the mass Biot number and the Thiele number are $Bi_{mo} = 10$ and $\Phi = 10$, respectively. In case 1c the mass Biot number is increased to $Bi_{mo} = 181$, and the Thiele number is held constant at $\Phi = 10$. Finally, in case 1d, the Thiele number is decreased to $\Phi = 0.2$, and the mass Biot number is held constant at $Bi_{mo} = 181$. The latter case represents sorption properties of Darco® G60 carbon blacks at a temperature of $T = 500$ K.

2.4.2 Numerical Specifications

The governing fluid transport equations are solved using a MacCormack-based finite difference scheme [14, 67]. The accuracy of the scheme is second order in time and fourth order in space. A first order accurate forward difference scheme is used to solve for the particle position, velocity, and mass as a function of time. The number of particles in the domain is $N_p = 50,000$. Since the fluid–particle transport equations are solved in a mixed Eulerian/Lagrangian framework, respectively, an interpolation algorithm is required to obtain the fluid transport variables at the particle locations. To this end, a linear interpolation scheme is used. Computations are performed on a domain of $2\pi \times 2\pi \times 1.2\pi$ in x , y , and z directions, respectively. Periodic boundary conditions are used in x and z directions, while free-stream boundary conditions are applied in y direction at the upper and lower boundaries of the domain, that is, the y -velocity component and the first derivative of all other transport variables vanish. The periodic conditions imply that fluid and particles, exiting through the left, right, rear, or front boundary, are reintroduced through the opposite boundary. The computational grid is comprised of $512 \times 512 \times 320$ evenly spaced grid points [19, 44].

2.4.3 Fluid Field and Particle Dispersion

The initial conditions are chosen such that four vortices are formed in streamwise direction. After the onset of the simulation, at time $t = 3$, a first vortex pairing is observed. Subsequently, the flow breaks up into smaller scales and grows in the nonperiodic direction, y , perpendicular to the mixing layer. Figure 2.6 shows an iso-surface of vorticity magnitude, $|\omega| = 1$, along with particle locations at four different times, obtained in case 1a. For purposes of illustration, only a subset of the domain is shown. Figure 2.6a reveals that, at time $t = 5$, particles accumulate in the periphery of the vortex and are thus entrained into the upper stream by means of large-scale mixing. Figure 2.6b and c illustrate the formation of streamwise vortical structures and continuous entrainment of particles into the upper stream at time $t = 10$ and $t = 20$, respectively. The simulation is stopped at time $t = 30$ before the size of the eddies becomes too large to be contained within the flow domain.

The effect of the unsteady flow field on particles with different Stokes numbers is illustrated in Fig. 2.7. Instantaneous vorticity contours are shown in the xy -plane, at $z = 0$, along with particle locations at time $t = 5$ and $t = 30$, obtained in case 1a and case 3. The vorticity fields are identical in both cases, as the particles do not affect the flow field [76, 77]. The particle dispersion patterns, however, are different. The particles in the $St_k = 0.17$ flow (case 1a) follow the fluid motion more closely than those in the $St_k = 10$ flow (case 3). Figure 2.7a reveals that, at time $t = 5$, particles in the $St_k = 0.17$ flow are engulfed in the growing vortices. By contrast, Fig. 2.7b shows that, at the same time, only few particles with $St_k = 10$ are carried along by the eddies. At time $t = 30$, a preferential concentration of $St_k = 0.17$ particles is observed, aligned with vorticity contours. Particles with Stokes numbers much larger than unity do not exhibit this behavior [42, 107].

Figure 2.8 provides insight into particle dispersion parallel to the mixing layer or the orientation of the particles with streamwise flow structures. Instantaneous vorticity contours and particle positions are shown in the xz -plane, at $y/\pi = -0.2$, obtained in case 1a and case 3 at time $t = 30$. Figure 2.8a reveals that particles with $St_k = 0.17$ preferentially collect in regions of low vorticity, as was pointed out earlier by other researchers [55, 107]. Figure 2.8b shows that particles with $St_k = 10$ (case 3) exhibit distinct streamwise patterns, although the alignment with low vorticity regions is not as pronounced as in the $St_k = 0.17$ flow.

A more quantitative measure of particle dispersion across the mixing layer is the probability density function (pdf) of the particles migrating into the upper, condensable vapor-containing, stream. The pdfs of the particle y -location, $f(y_p)$, for all cases are shown in Fig. 2.9 at four different times. The dot-dashed line indicates the initial condition, with all particles being uniformly distributed in the lower stream, $-1 \leq y_p/\pi \leq 0$, where $f(y_p)$ is unity. The pdfs obtained in case 1a and case 2 are almost identical, implying that the nondimensional particle relaxation time, St_k/f_p , is approximately equal in both cases, even though the reference particle Reynolds number, Re_{p0} , differs. Figure 2.8a shows that, at time $t = 5$, only a small fraction (0.6%) of the particles in the $St_k = 10$ flow (case 3) have entered the

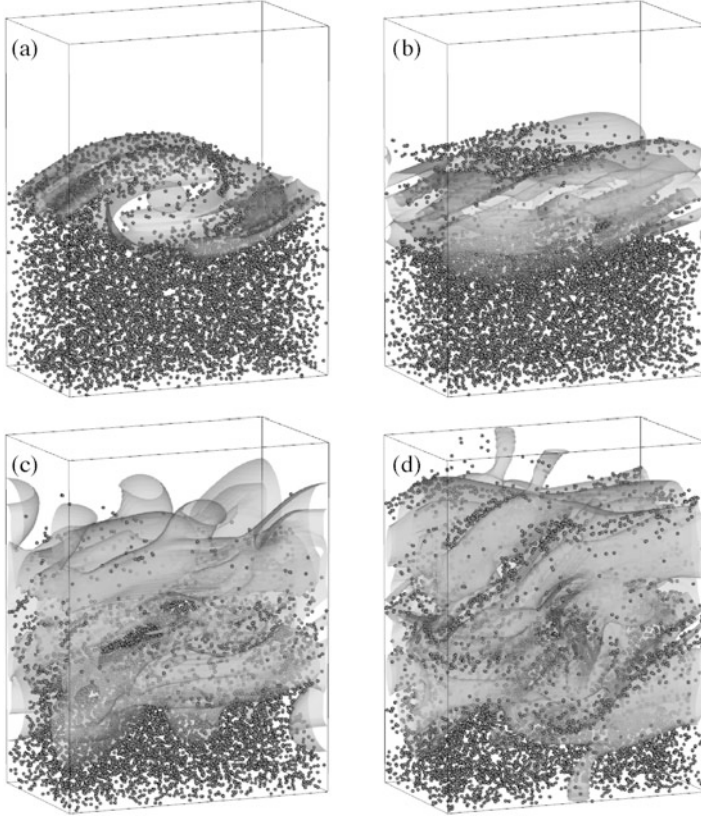


Fig. 2.6 Instantaneous vorticity magnitude iso-surface, $|\omega| = 1$, and particle locations, obtained in case 1a at time: (a) $t = 5$; (b) $t = 10$; (c) $t = 20$; (d) $t = 30$. The domain range shown is $0 \leq x/\pi \leq 1$, $-2 \leq y \leq 2$, and $0 \leq z/\pi \leq 0.6$

upper stream. At the same time, an order of magnitude more particles (6%) in the $St_k = 0.17$ flows (cases 1a and 2) are entrained by the upper stream. At time $t = 10$, Fig. 2.9b shows an accumulation of particles in the $St_k = 0.17$ flows at the periphery of the eddies, near $y_p/\pi = \pm 0.2$. Figure 2.9c shows that the fraction of particles in the upper stream of the $St_k = 0.17$ flow remains nearly constant and does not exceed 6% until time $t = 20$. At time $t = 30$, Fig. 2.9d shows that the number of particles entrained by the upper stream is approximately twice as much in cases 1a and 2 than in case 3.

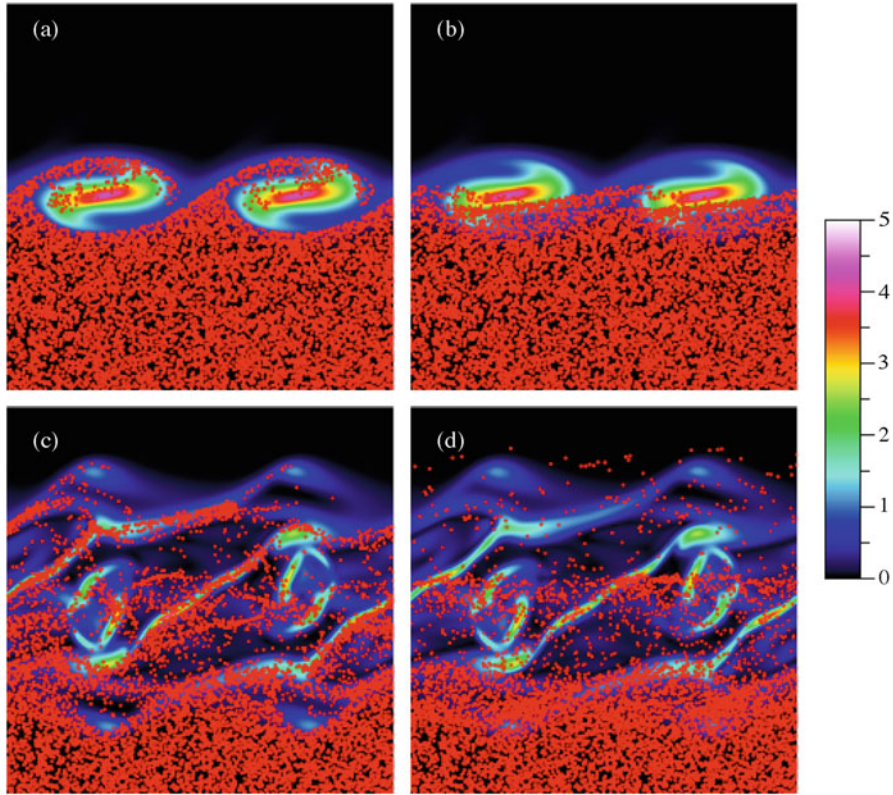


Fig. 2.7 Instantaneous vorticity magnitude contours and particle locations in the xy -plane at $z = 0$: (a) case 1a, time $t = 5$; (b) case 3, $t = 5$; (c) case 1a, $t = 30$; (d) case 3, $t = 30$

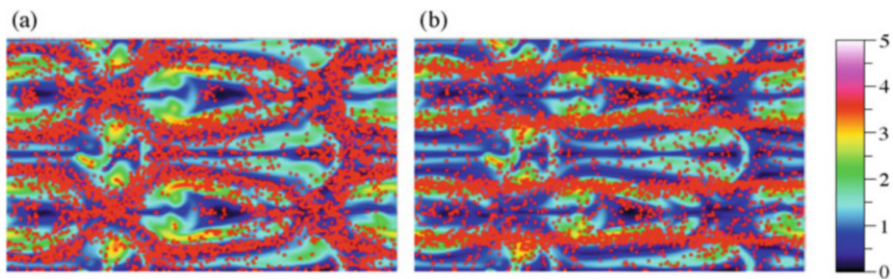


Fig. 2.8 Instantaneous vorticity magnitude contours and particle locations in the xz -plane at $y/\pi = -0.2$ and time $t = 30$: (a) case 1a; (b) case 3

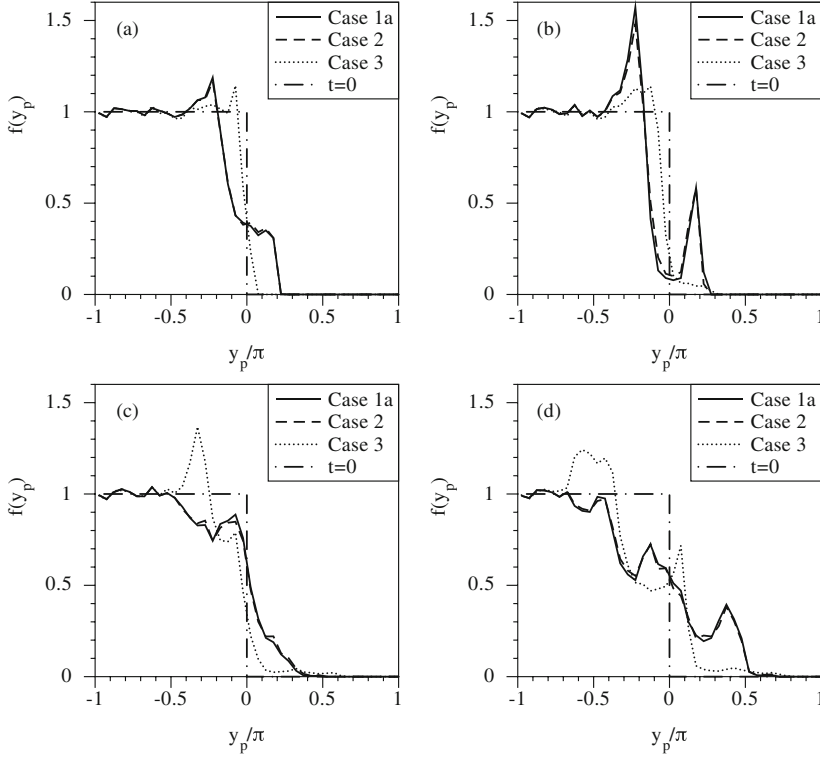


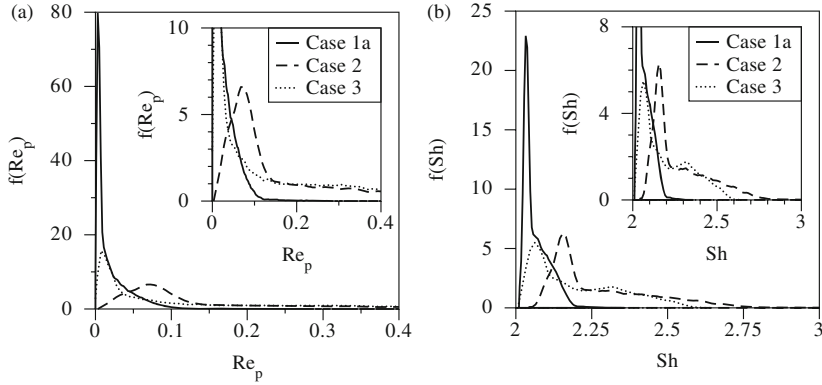
Fig. 2.9 Instantaneous pdfs of the particle y -location, $f(y_p)$, at time: (a) $t = 5$; (b) $t = 10$; (c) $t = 20$; (d) $t = 30$

2.4.4 Mass Transfer

The Sherwood number, Sh , is a governing parameter for gas–particle mass transfer. It accounts for the diffusive flux as well as the increased mass transfer due to a gas–particle slip velocity, Δu_i . The Sherwood number is modeled as a function of the particle Reynolds number, Re_p , which in turn depends on Δu_i (2.8). Research has shown that the particle slip velocity grows with increasing Stokes numbers [95]. The lower the Stokes number, the more closely particles follow streamlines and the lower the gas–particle slip velocity becomes. The gas–particle slip velocity vanishes in the limiting case of $St_k \rightarrow 0$. Hence, particles in the $St_k = 10$ flow (case 3) exhibit a higher gas–particle slip velocity than those in the $St_k = 0.17$ flows (case 1a and case 2). The mean gas–particle slip velocities for particles with $St_k = 0.17$ are $|\overline{\Delta u_i}| = 0.014$ and $|\overline{\Delta u_i}| = 0.013$ in case 1a and case 2, respectively. (An overline denotes a quantity averaged over all particles at time $t = 30$.) The difference can be attributed to a different reference particle Reynolds number, which has an influence on the particle motion through the drag correction

Table 2.2 Mean quantities, surface concentration, and overall mass removal for cases 1a–d, case 2, and case 3

Case	1a	1b	1c	1d	2	3
Slip velocity, $ \Delta u_i $	0.0145	0.0145	0.0145	0.0145	0.0134	0.1431
Reynolds number, $\overline{Re_p}$	0.0191	0.0191	0.0191	0.0191	0.3405	0.1894
Sherwood number, \overline{Sh}	2.0663	2.0663	2.0663	2.0663	2.2813	2.2014
Surface concentration, $c_s(Bi_{mo}, \Phi)$	0	0.5263	0.9527	0.9999	0	0
Mass removal, $\Theta(t = 30)$	7.8%	4.3%	0.5%	<0.1%	23.6%	8.5%

**Fig. 2.10** Instantaneous pdfs of (a) the particle Reynolds number, $f(Re_p)$, and (b) the Sherwood number, $f(Sh)$, at time $t = 30$

factor, f_p . For particles with $St_k = 10$ (case 3), the mean gas–particle slip velocity is $|\Delta u_i| = 0.1431$, which is one order of magnitude larger than the $St_k = 0.17$ cases. Mean quantities are listed in Table 2.2.

Figure 2.10a shows pdfs of the particle Reynolds number, $f(Re_p)$, which is related to the gas–particle slip velocity through $Re_p = |\Delta u_i|Re_{po}$. As a result of the augmented particle slip velocity in case 3, the mean particle Reynolds number is larger in case 3 than in case 1a. The largest particle Reynolds numbers, Re_p , are observed in case 2, owing to the large reference particle Reynolds number, $Re_{po} = 25.3$. However, the particle Reynolds numbers are less than unity even in case 2, which results in a drag correction of less than 15% (i.e., $f_p - 1 < 0.15$) and explains why there is no significant difference in terms of particle dispersion between case 1a and case 2. It is therefore adequate to use Stokes law to describe particle motion. The mean particle Reynolds numbers are $\overline{Re_p} = 0.02$, $\overline{Re_p} = 0.34$, and $\overline{Re_p} = 0.19$ in case 1a, case 2, and case 3, respectively. Finally, the pdfs of the Sherwood number, $f(Sh)$, are presented in Fig. 2.10b. The correlation between the Sherwood number and the particle Reynolds number is given by Eq. (2.8). Consequently, the mean Sherwood number is largest in case 2, intermediate in case 3, and smallest in case 1a. The pdfs $f(Sh)$ all have a distinctive left-skewed shape with a minimum value of $Sh = 2$, which corresponds to mass transfer in

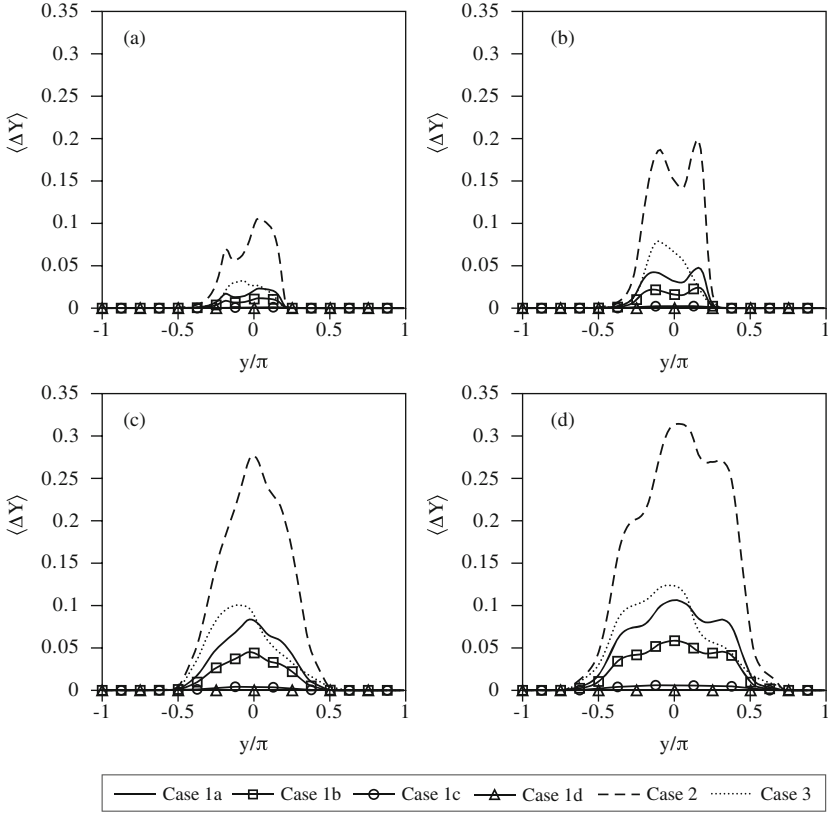


Fig. 2.11 Cross-stream profiles of the condensable vapor mass fraction removed from the fluid, $\langle \Delta Y \rangle$ at time: (a) $t = 5$; (b) $t = 10$; (c) $t = 20$; (d) $t = 30$

a stagnant fluid, purely due to diffusion. Convective effects at the particle surface, resulting from a non-zero particle slip velocity, become manifest in $Sh > 2$ values. Hence, on average, convective effects act to increase mass transfer by 3% in case 1a ($\bar{Sh}/2 = 1.033$), 14% in case 2 ($\bar{Sh}/2 = 1.14$), and 10% in case 3 ($\bar{Sh}/2 = 1.10$).

Cross-stream profiles of the vapor mass fraction removed by condensation, $\langle \Delta Y \rangle$, are presented in Fig. 2.11 for all cases at four different times. (The brackets $\langle \cdot \rangle$ denote a quantity averaged in x - and z -direction.) The ordinate spans across the height of the mixing layer $-1 \leq y/\pi \leq 1$. Profiles are obtained by comparing averaged species profiles, $\langle Y \rangle$, against a simulation without mass transfer. Initially, all particles are located in the region $y < 0$, and vapor is contained in the region $y > 0$ only. Figure 2.11a reveals that, at time $t = 5$, vapor is removed in the range $-0.5 \leq y/\pi \leq 0.25$ where particles mix with vapor. This range broadens with time, as particle dispersion increases and more vapor is entrained into the lower stream. It was shown in Fig. 2.9 that only few particles with $St_k = 10$ enter the upper stream. Consequently, mass is predominantly removed from the lower stream

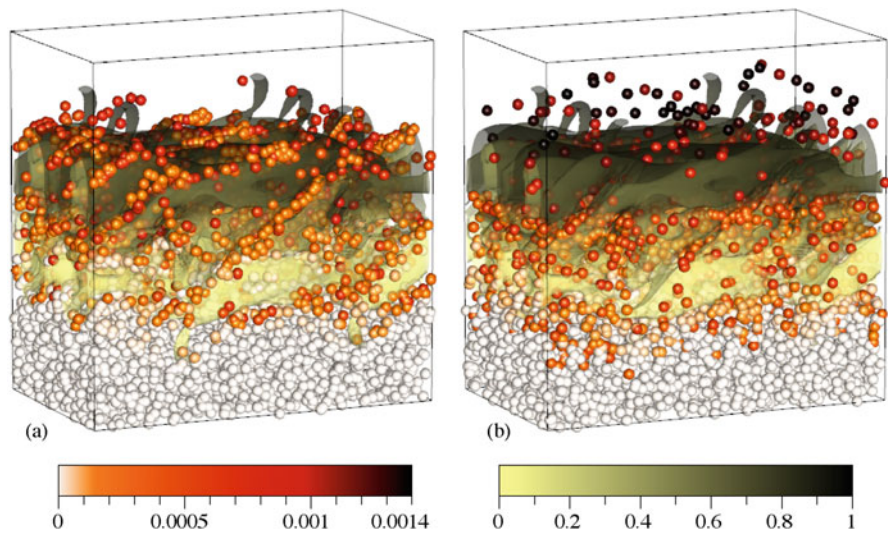


Fig. 2.12 Instantaneous vorticity iso-surface (magnitude = 1) and particle locations at time $t = 30$ in (a) case 1a and (b) case 3. Only 10,000 particles are shown for clarity. The iso-surface is colored based on the local vapor mass fraction. The *color* of the particles represents the mass of vapor accumulated on the particle

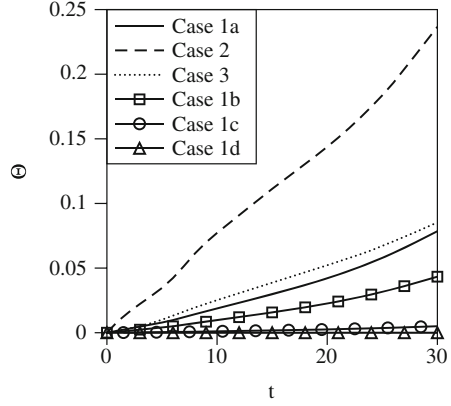
in case 3, which can be concluded from a left-skewed shape of the profile in that case. In all other cases, where particle dispersion is increased, more mass is removed from the upper stream. The highest mass removal is achieved in case 2, where the parameter A has a value of $A = 10^{-3}$. The lowest mass removal is observed in case 1d, where the surface concentration is $c_s = 0.9999$ owing to a large mass Biot number ($Bi_{mo} = 181$) and a small Thiele number ($\Phi = 0.2$), cf. Table 2.2.

A qualitative view of the particle transport and gas adsorption dynamics is shown in Fig. 2.12. The image shows the particle locations, mass captured by the particles, vapor mass fraction, and an iso-surface of vorticity. The results for case 1a are shown in Fig. 2.12a, and the results for case 3 are shown in Fig. 2.12b. The contortions of iso-surface ($|\omega| = 1.5$) reflect that the flow has transitioned to turbulence. The images reveal that the particles in case 3 have captured more vapor than those in case 1a. However the differences appear to be significant only for those particles that have migrated into the upper part of the domain. The increased Stokes number and particle Reynolds number (due to the greater slip velocity, Δu_i) increase the Sherwood number vis a vis Eq. (2.8).

The fraction of vapor removed from the fluid by condensation is given by

$$\Theta(t) = 1 - \frac{\int \int \int Y(x, y, z, t) dx dy dz}{\int \int \int Y(x, y, z, t = 0) dx dy dz}, \quad (2.10)$$

Fig. 2.13 Temporal evolution of the fraction of vapor, Θ , removed from the fluid



where $Y(x, y, z, t = 0)$ is the vapor mass fraction at time $t = 0$. The temporal evolution of Θ is presented in Fig. 2.13. The highest vapor removal is observed in case 2. This can be attributed to two separate effects: firstly, to an increased mass transfer rate due to convection (high \bar{Sh}) and, secondly, to the large value of the parameter A . The amount of vapor removed at time $t = 30$ is listed in Table 2.2 for all cases. Particles with $St_k = 10$ (case 3) remove more vapor than particles with $St_k = 0.17$ (case 1a) as a result of an increased gas–particle slip velocity. The lowest removal is achieved in cases 1b, 1c, and 1d, where the perfect sink assumption is not used and hence the surface concentration approaches a value of $c_s = 1$. The results presented in Figs. 2.11 and 2.13 emphasize that mass removal is greatly overpredicted if the perfect sink assumption is used.

2.5 Summary and Conclusions

In this chapter, we considered gas-to-particle mass transfer in turbulent flows. We performed DNS of round jets and temporal mixing layers. The round jet simulations mimic the nozzle region in ACI while the temporal mixing layer allows us to perform high-resolution simulations and capture the fluid–particle interactions in more depth. All flows consisted of a particle-laden stream, initially containing uniformly distributed particles, mixing with a particle-free stream containing condensable vapor. The fluid field was obtained by solving the incompressible Navier–Stokes equations in a Eulerian frame of reference, while a Lagrangian formulation was used to describe particle motion. The fluid and particle fields were coupled through gas–particle mass transfer of condensable vapor.

The jet simulations reveal the dynamics of the 0.1, 1, and 10 μm diameter porous particles. We quantified the effect of particle size on particle Reynolds numbers—the nondimensional parameter determining drag/dispersion and mass transfer. While the smaller particles are more readily dispersed across the span of the flow, and in the vortices, it is the larger particles that exhibit the greatest slip or relative velocities. This increased slip velocity results in increased condensation mass transfer.

The temporal mixing layer simulations revealed that the overall mass removal rate increases when the parameter A is increased. An increase in A corresponds to an increase in the diffusive mass transfer to the particle surface. Additionally, it was shown that mass removal is overpredicted if the perfect sink assumption is used. From an engineering point of view, mass transfer can be increased in several ways: (1) increasing the gas–particle slip velocity, (2) increasing the specific particle surface area, or (3) using highly reactant sorbent particles (large Thiele numbers). The computational model presented in this work can be used to predict condensation mass transfer under turbulent flow conditions. Unlike previous studies, it accounts for increased mass transfer due to convective effects in the boundary layer of the particles.

Unfortunately the use of DNS to simulate turbulent flows in industrial scale ductwork is yet out of reach from a computational expense point of view. Alternative modeling strategies are needed for use in the industrial engineering context. The techniques need to be capable of describing/capturing particle motion and gas-to-particle mass transfer in a sufficiently accurate manner.

Modeling of Gas-to-Particle Mass Transfer in Turbulent
Flows

Garrick, S.C.; Bühlmann, M.

2018, XII, 61 p. 33 illus., 15 illus. in color., Softcover

ISBN: 978-3-319-59583-2